Cell Reports
Physical Science

CellPress
OPEN ACCESS

Report

Vanadium Oxide Clusters Decorated Metallic Cobalt Catalyst for Active Alkaline Hydrogen Evolution

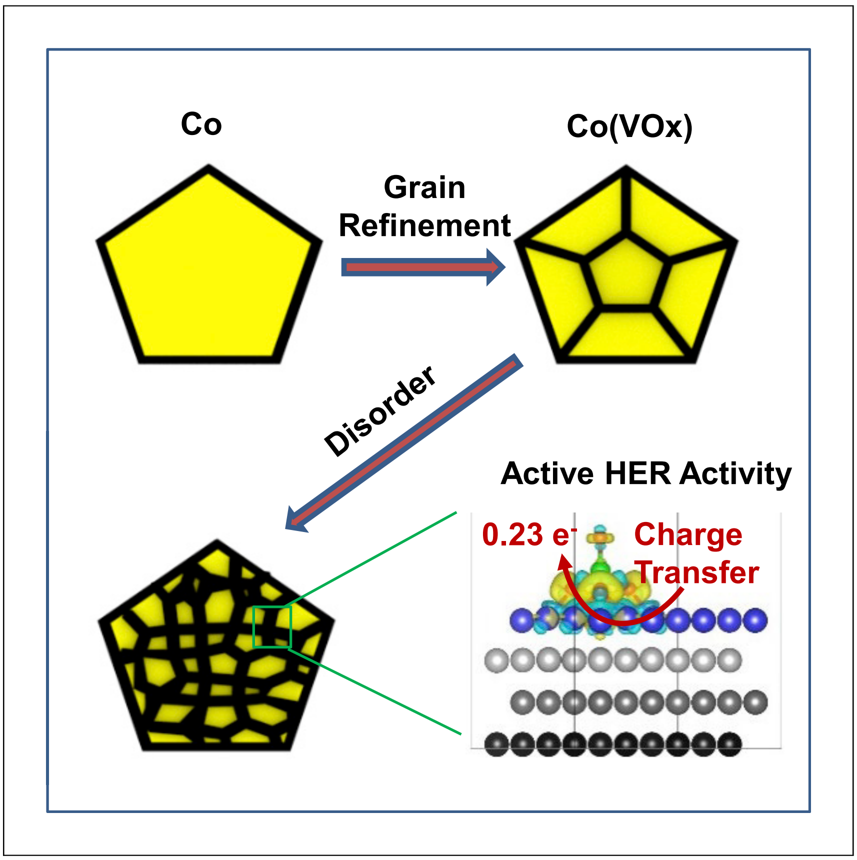

Fe triad elements (Fe, Co, and Ni) are commonly used as catalysts for many hydrogenation applications. Here, Li et al. report a highly active Co(VOx) catalyst with disordered lattice and downsized particle size for H_2 evolution. The approach can potentially be extended to treat other transition-metal-based materials for efficient H_2 production.

Yibing Li, Xin Tan, Wanfeng Yang, ..., Tingwen Zhao, Sean C. Smith, Chuan Zhao

chuan.zhao@unsw.edu.au

HIGHLIGHTS

VOx clusters endow Co highly disordered lattice and downsized particle size

VOx clusters enable efficient electron transfer from Co to VOx

Co(VOx) catalyst exhibits notable alkaline HER activity and robust stability

Li et al., Cell Reports Physical Science *1*, 100275
December 23, 2020 © 2020
https://doi.org/10.1016/j.xcrp.2020.100275

Cell Reports
Physical Science

Report

Vanadium Oxide Clusters Decorated Metallic Cobalt Catalyst for Active Alkaline Hydrogen Evolution

Yibing Li,[1,3] Xin Tan,[2,3] Wanfeng Yang,[1] Xin Bo,[1] Zhen Su,[1] Tingwen Zhao,[1] Sean C. Smith,[2] and Chuan Zhao[1,4,*]

SUMMARY

Promoting active and stable H_2 evolution reaction (HER) on metallic Fe triad materials is important yet challenging. Here, we report a metallic Co catalyst modulated by vanadium oxide (VOx) clusters (denoted as Co(VOx)) for active alkaline HER activity. Systematic X-ray absorption spectroscopy (XAS) and X-ray crystallography studies verify that VOx clusters endow Co with a highly disordered lattice and downsized particle size. The best Co(VOx) electrode is achieved with an optimal doping level of 3%, which delivers −100 mA cm^{-2} at an overpotential merely of 178 mV, in contrast to 344 mV and continuous activity decay on pure Co. The lower or higher doping level is unable either to regulate the atomic structure and reduce the H binding or to provide fewer active sites. Density functional theory (DFT) calculations reveal that VOx enables efficient electron transfer from Co to VOx, thus decreasing the H-adsorption on V-Co(001) for enhanced HER.

INTRODUCTION

H_2 is considered an ideal clean energy carrier to replace traditional fossil fuels.[1–4] Electrocatalytic H_2 evolution reaction (HER) from renewable energy by water splitting is a promising technology for efficient H_2 production.[5–8] Various Earth-abundant metal-based catalysts with considerable HER activities have been broadly reported to replace precious platinum group metal (PGM) electrocatalysts.[9–14] Unfortunately, a large gap still exists between non-precious metals and PGM catalysts toward HER, owing to the lack of efficient active sites. The occurrence of too weak (e.g., for Cu and Zn) or too strong (e.g., for Co, Ni, and W) H adsorption results in a lower reaction rate through affecting the initial H adsorption and/or the ultimate molecular H_2 desorption from the catalyst surface.[15] In particular, metallic Ni and its alloys are widely regarded as the most promising non-precious-metal electrocatalysts alternative to PGM for industrial-scale water electrolysis; yet, the strong H adsorption on Ni has severely affected its durability.[16]

The Fe triad elements (i.e., Fe, Co, and Ni) share similar chemical and physical characteristics, are abundant on Earth, and have been popularly used as catalysts for many hydrogenation applications.[17,18] For example, metallic Co is the most widely used catalyst in Fischer-Tropsch synthesis (FTS) for converting H_2 and carbon monoxide from coal or natural gas into long-chain hydrocarbons.[19,20] However, metallic Co and Fe typically show poor activity toward HER, although Co- and Fe-based chalcogenides,[21] nitrides,[22] carbides,[23] and phosphides,[24] and their interaction with heteroatom-doped carbon and macrocyclic Co complexes[25,26] have been reported

[1]School of Chemistry, Faculty of Science, University of New South Wales, Sydney, NSW 2052, Australia

[2]Integrated Materials Design Laboratory, Department of Applied Mathematics, Research School of Physics, The Australian National University, Canberra, ACT 2601, Australia

[3]These authors contribute equally

[4]Lead Contact

*Correspondence: chuan.zhao@unsw.edu.au

https://doi.org/10.1016/j.xcrp.2020.100275

as having considerable activity for HER. Co can exist in two crystallographic structures: the hexagonal close packed (*hcp*) and the face-centered cubic (*fcc*) phase. Many reports have revealed that the *hcp* Co is more active than *fcc* Co, due to the intrinsic stacking faults that offer a greater number of active sites.[27,28] Nevertheless, the large size of nanoparticles (NPs) with limited surface area and strong H binding over Co greatly slow down the desorption of H to evolve H_2 and limit the HER kinetics. To achieve enhanced HER catalytic performances on Co, downsizing the catalysts to fine NPs and creating disordered structure to engender more exposed active sites, along with optimized electronic structures for H binding, are critical.

Here, we show a *hcp* metallic Co catalyst modulated by vanadium oxide (VOx) clusters (denoted as Co(VOx)) with extraordinary HER activity as well as an atomic-level understanding of the activity origins. The VOx-modulated metallic Co catalyst ((Co(VOx)-y, y is the V^{5+}/Co^{2+} precursor molar ratios) is prepared by a facile electrodeposition process. Due to the strong interaction between Co and VOx, the crystallographic, electronic structure, and coordination environment can be rationally regulated at atomic scale by adjusting the doping levels during the electrodeposition process. The VOx doping plays an important role for achieving a refined Co NPs and highly disordered Co structure. The optimal Co(VOx)-3% catalyst exhibits extraordinarily low overpotentials and high activity and stability toward HER, which are distinctly different from the poor HER activity and durability of metallic Co. X-ray absorption spectroscopy (XAS), X-ray crystallography, operando Raman spectroscopy, and density functional theory (DFT) calculations are applied to study the roles of VOx clusters, uncovering the highly disordered structures and partial electron transfer from Co to VOx, which dramatically decreases the H adsorption on V-Co(001) to achieve enhanced HER.

RESULTS AND DISCUSSION

Catalyst Synthesis and Physical Characterization

The Co(VOx)-y (y = 0%, 1%, 3%, and 6%) catalysts with different doping levels are electrodeposited directly on Ni foam (NF) substrate, and all of the electrodes after electrodeposition show a black color. The X-ray diffraction (XRD) pattern of Co and Co(VOx) samples electrodeposited on carbon fiber paper to remove the effect of diffraction signals from NF were collected by using the Empyrean PANalytical diffractometer in the grazing incidence measurement mode. As shown in Figure 1D, for pure Co, the characteristic peaks located at 41.5°, 44.5°, and 47.3° are indexed to the (100), (001), and (101) planes of *hcp* metallic Co (joint committee on powder diffraction standards [JCPDS]: 05-0727),[20] respectively. VOx doping has a remarkable influence on the crystal structure of Co. With the increment of VOx doping, the two characteristic peaks at 41.5° and 47.3° almost disappear, while the (001) peak broadens and decreases sharply, indicating the formation of a poorly crystallized Co structure and refined NPs, as illustrated in Figure 1A.

To identify the structural transformation of Co by VOx doping, the electrodeposition behavior of the Co(VOx)-y electrodes was analyzed. The representative Co(VOx)-3% electrode is discussed in the following sections, unless stated otherwise, as it shows the highest HER activity. Figure S1 shows that pure Co was electrodeposited at a more positive potential than that for pure VOx deposition from the NH_4VO_3 precursor. However, the deposition of VOx can significantly influence the Co crystallization, as evidenced by a negative shift of the electrodeposition potential for Co(VOx)-3%. This negative shift in potential indicates that VOx regulates the nucleation and crystallization process of metallic Co. Because the formed VOx are ultrafine NPs in

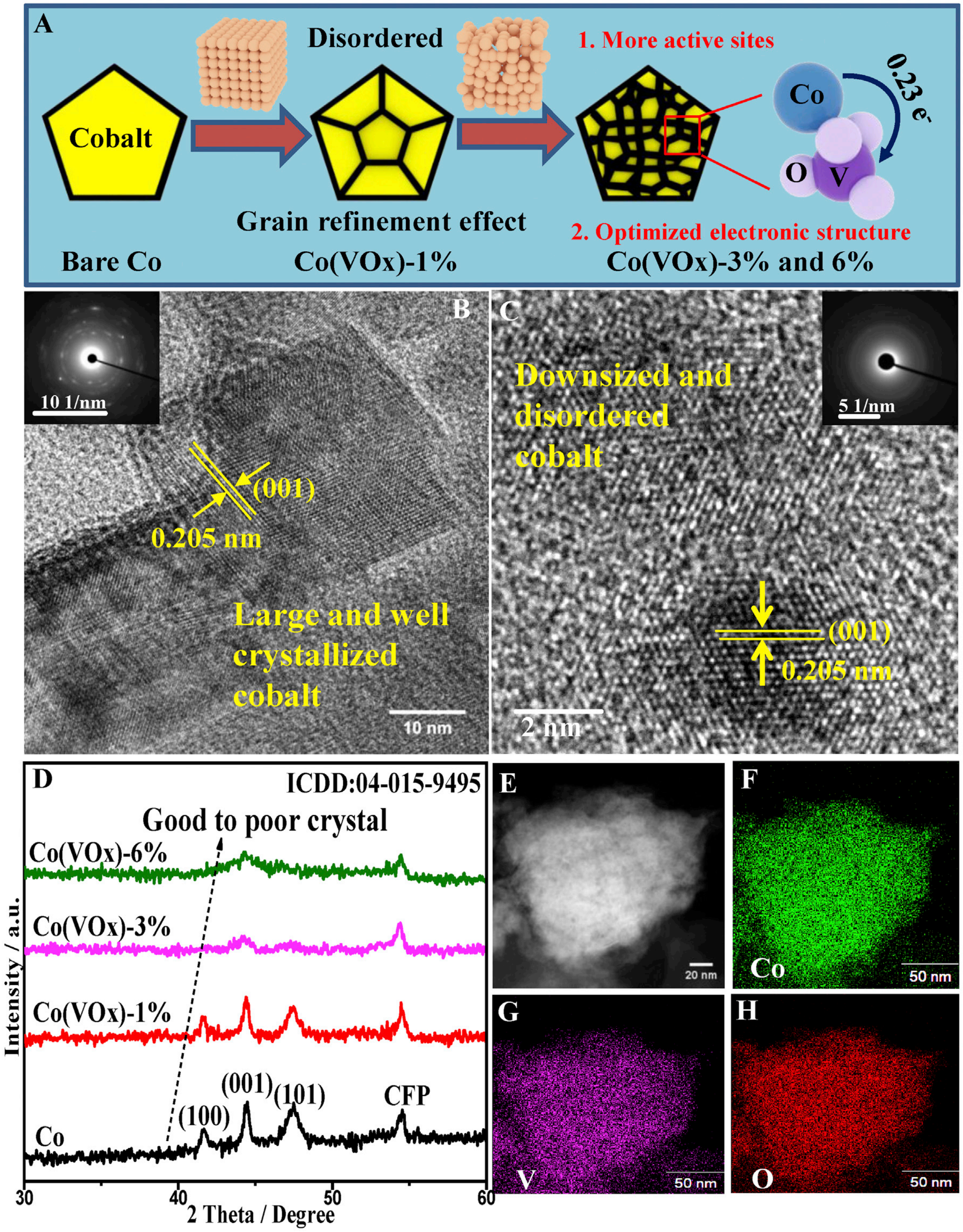

Figure 1. Sample Preparation Schematic and Morphology

(A) Schematic illustration of the VOx effect on Co for enhanced HER.

(B and C) HRTEM and SAED pattern (inset) for pure Co and Co(VOx)-3% electrodes.

(D) XRD pattern of the prepared Co-based samples.

(E–H) TEM-EDS elemental mapping of the Co(VOx)-3% sample.

nature (see scanning electron microscopy [SEM] information below), thus, the crystallization structure and size of Co can be well regulated by VOx.

The morphology of the obtained catalysts was first characterized by SEM. Figure S2 shows the SEM image of uniformly and densely distributed Co NPs on NF. At high magnifications, it is revealed that the size of NPs is in the scale of tens of nanometers. For the electrodeposited VOx, the NF substrate is uniformly covered with the composite constituted by a large number of NPs with sizes of merely several nanometers (Figure S3). Figure S4 depicts the different magnified SEM morphology for Co(VOx)-3% with respect to the individually deposited Co or VOx. In the presence of vanadium, the well-ordered structure of Co NPs was transformed into an irregular nanocluster structure composed of fine NPs with a size of few nanometers, indicating the crystalline refinement effect of VOx on Co. Transmission electron microscopy (TEM) was used to learn more about the structure of Co(VOx) composites. As seen in Figures 1B and S5, the TEM morphology of pure Co shows large NPs with sizes ranging ~30–50 nm. The clear lattice patterns and diffraction rings from the selected area electron diffraction (SAED; inset in Figure 1B) both indicate the well-crystallized Co structure. The TEM images of the Co(VOx)-3% sample reveal the uniformly distributed fine NPs structure with a size of ~5–10 nm (Figure 1C). The high-resolution TEM (HRTEM) image in Figure 1C shows a lattice fringe of 0.205 nm, which is consistent with the (001) plane of Co and corresponds well with the SAED pattern (Figure 1C, inset). However, the poorly defined rings in SAED demonstrate the poor crystalline phases and a disordered Co structure. The elemental distribution was confirmed by TEM-energy dispersive spectroscopy (EDS) mapping, in which all the elements are uniformly distributed throughout the whole sample (Figures 1E–1H). In addition, the HRTEM morphologies of Co(VOx)-1% and Co(VOx)-6% samples (Figures S6 and S7) depict Co NPs with sizes between ~15–20 nm and ~5–10 nm with good and poor lattice fringe for Co (001) plane, respectively, demonstrating that both the morphology and crystal structure of Co NPs can be well tuned through VOx modulation.

X-ray photoelectron spectroscopy (XPS) was used to investigate the valence states of the as-prepared Co and Co(VOx) samples. As seen from Figure S8, in the Co2p region, the two main peaks for Co2p3/2 and Co2p1/2 are located at 781.2 eV and 797.3 eV, accompanied by two shake-up satellite peaks (786.6 eV and 803.1 eV), demonstrating an oxidized Co surface. In addition, an enhanced oxidation degree of Co after the increment of the doped VOx causes a slightly negative energy shift in Co2p configuration.[29] The high-resolution XPS of the V2p region shows characteristic peaks at 517.1 eV and 516.4 eV assigned to V^{5+} and V^{4+} species,[30] and a slightly negative shift of V2p was observed with increasing VOx doping. The energy shift on Co2p and V2p reveals a direct interaction between Co and VOx and a charge transfer from Co to VOx.[31] The O1s XPS spectra show a main peak at ~531.1 eV, corresponding to O in VOx and the oxidized Co-O in the composite. It is noted that the metallic Co peaks were not observed in the XPS spectra because of the surface oxidized layers.

Electrochemical H_2 Evolution Activity Investigation

The HER performance of the as-prepared Co(VOx) catalysts with different VOx concentrations (0%–6%) along with the commercial 20 wt % Pt on carbon black (Pt/C) electrodes are evaluated in 1 M KOH without ohmic potential drop (iR) correction (Figure 2A). Linear sweep voltammetry (LSV) of all the prepared Co(VOx) electrodes show significantly enhanced HER activity compared to the bare Co electrode. In particular, the Co(VOx)-3% electrode shows the best HER activity, suggesting the

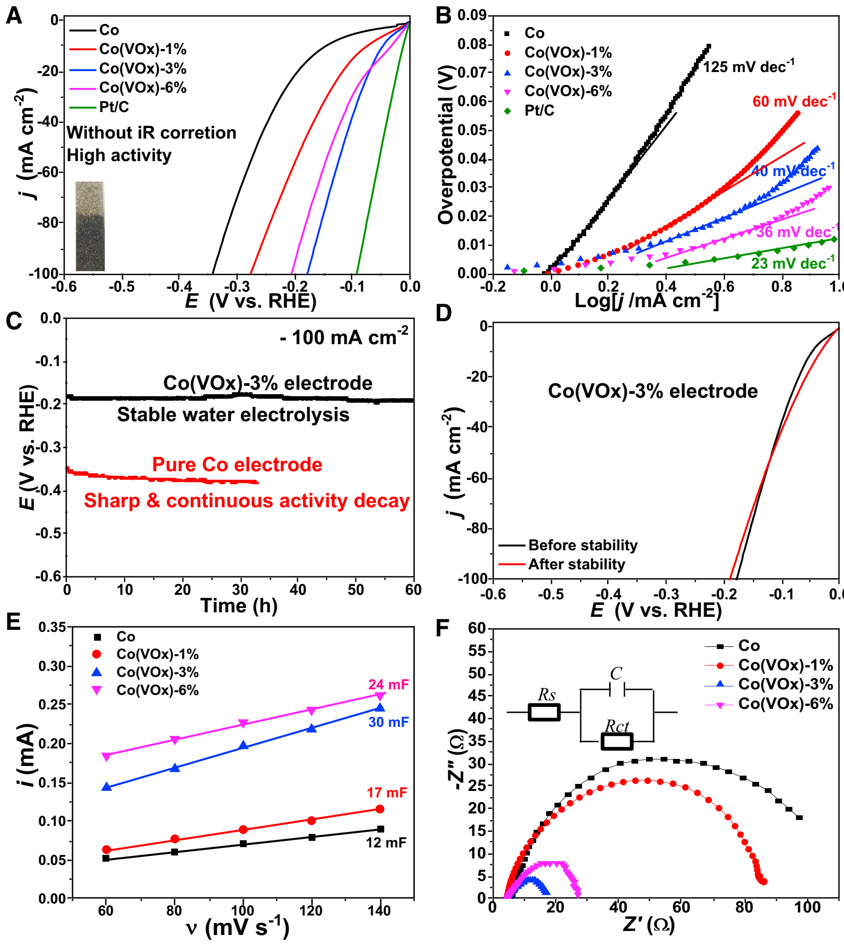

Figure 2. Electrochemical Characterization of the Co(VOx) Electrodes

(A and B) The LSV polarization curves on the prepared electrodes (without iR correction) and corresponding Tafel plots; the inset image in (A) is the prepared Co(VOx)-3% electrode.

(C) Time dependence of current densities at -100 mA cm^{-2} on Co(VOx)-3% and pure Co electrodes.

(D) The LSV curves of the Co(VOx)-3% electrode before and after stability test.

(E and F) Extraction of the C_{dl} and the EIS spectra of the prepared electrodes.

electrodeposited VOx with optimal doping plays an important role in the activity enhancement. Specifically, to deliver a current density of -100 mA cm^{-2}, the Co(VOx)-3% electrode requires an overpotential of merely 178 mV, which is much smaller than 344 mV and 275 mV required for Co and Co(VOx)-1%, respectively, and 203 mV for Co(VOx)-6%. The obtained performance of Co(VOx)-3% is comparable or outperforms recently reported state-of-the-art noble-metal-free HER catalysts, although it still shows a larger overpotential than Pt/C catalyst (93 mV) (Table S1). The corresponding Tafel slopes were derived from the LSV curves to investigate the reaction kinetics. As shown in Figure 2B, the Co(VOx)-3% and Co(VOx)-6% electrodes have similar Tafel slopes of 40 and 36 mV dec^{-1}, respectively, which are much smaller than those of Co(VOx)-1% (60 mV dec^{-1}) and Co (125 mV dec^{-1}), suggesting that HER follows the Volmer-Heyrovsky mechanism at the Co(VOx) electrodes. Also, a Tafel slope of 23 mV dec^{-1} was obtained for the Pt/C electrode. The significantly decreased Tafel slope of Co(VOx)-3% and Co(VOx)-6% indicate fast intrinsic kinetics of HER due to the formation of the fine and disordered Co structure (see below).

The long-term electrocatalytic durability is a pivotal parameter for a HER electrode. Figure 2C shows that the Co(VOx)-3% catalyst retains a stable HER activity for over 50 h. In contrast, the bare Co electrode shows a noticeable activity decay during the continuous HER operation. Additionally, the almost overlapped LSV curves obtained on the Co(VOx)-3% electrode before and after stability demonstrate the robustness of the Co(VOx)-3% electrode (Figure 2D). The stable activity of the catalyst was further studied by the post-HER characterizations. As shown in Figure S9, the almost unchanged morphology of the fine NPs and the retained uniform distribution of the constituting elementals both indicate the rigid structure of the Co(VOx)-3% catalyst, and the HRTEM also reveals the existence of the lattice fringe for metallic Co.

To understand the origin of the enhanced HER activity on Co(VOx) catalysts, the electrochemical active surface area (ECSA) was first determined by measuring the double-layer capacitance (C_{dl}) of the electrodes derived from cyclic voltammetry (CV) curves in a non-Faraday region with different sweep rates (Figure S10).[32] The C_{dl} values obtained on Co(VOx) electrodes are all larger than that on pure Co (12 mF), with the Co(VOx)-3% electrode being the largest (30 mF), followed by Co(VOx)-6% (24 mF) and Co(VOx)-1% (17 mF) (Figure 2E). These results demonstrate that the fine NPs and disordered structure provide more active sites for HER. Moreover, the intrinsic catalytic activity of each active site was evaluated by normalizing current against ECSA. Figure S11 shows that the Co(VOx)-3% electrode still exhibits a higher HER activity than Co and Co(VOx)-1%, demonstrating the profound role of VOx in enhancing the intrinsic activity of each active site. It should be noted that the ECSA normalized HER activity of Co(VOx)-3% and Co(VOx)-6% electrodes almost overlapped, suggesting that the more exposed active sites are contributing in the improved HER on Co(VOx)-3%, and this observation is consistent with the projected DFT simulations (see below). In addition, the charge transfer process of the prepared samples was investigated by electrochemical impedance spectroscopy (EIS), and an equivalent resistor-capacitor circuit model (R_s, resistor; R_{ct}, charge transfer resistance; C, capacitance) was used to fit the impedance spectra. As shown in Figure 2F, the EIS spectra reveal a significantly smaller R_{ct} for the Co(VOx)-3% electrode (12 Ω) than that of Co(VOx)-6% (22 Ω), Co(VOx)-1% (81 Ω), and Co (107 Ω), verifying the fast electron transfer kinetics of HER on Co(VOx)-3%. Furthermore, the Faradaic efficiency close to unity is obtained on the Co(VOx)-3% electrode by measuring the generated H_2 gas by using gas chromatography (Figure S12).

XAS and Operando Raman Spectroscopy for Structure Analysis

To obtain further information on the elemental oxidation states and in particular to determine the influence of VOx on the atomic structure of Co and eventually the HER performance, the Co K-edge X-ray absorption near edge structure (XANES) was studied in detail. As seen from Figure 3A, the XANES spectra of Co and Co(VOx)-1% contain similar pre-edge characteristic features, referring to an oxidation state close to metallic Co for Co in these catalysts. With increasing the VOx amount, both the positively shifted pre-edge peak and higher white line intensity demonstrate a higher oxidation degree of Co (Figure 3B). In other words, the Co(VOx)-3% and Co(VOx)-6% catalysts are oxidized and disordered more at higher VOx doping levels. Figure 3C shows the resulting Fourier-transformed extended X-ray absorption fine structure (FT-EXAFS) for all prepared samples. There are fewer scattering contributions from the Co-O bond for Co and Co(VOx)-1%, but the other three nearest-neighbor (NN; 2nd–4th) shells show strong intensity, which indicates the formation of metallic Co with highly ordered atomic structure.[33] It should be noted that from XPS spectra, we observed that these two samples are oxidized, but the XAS spectra reveal a metallic phase structure. This is because XPS is a

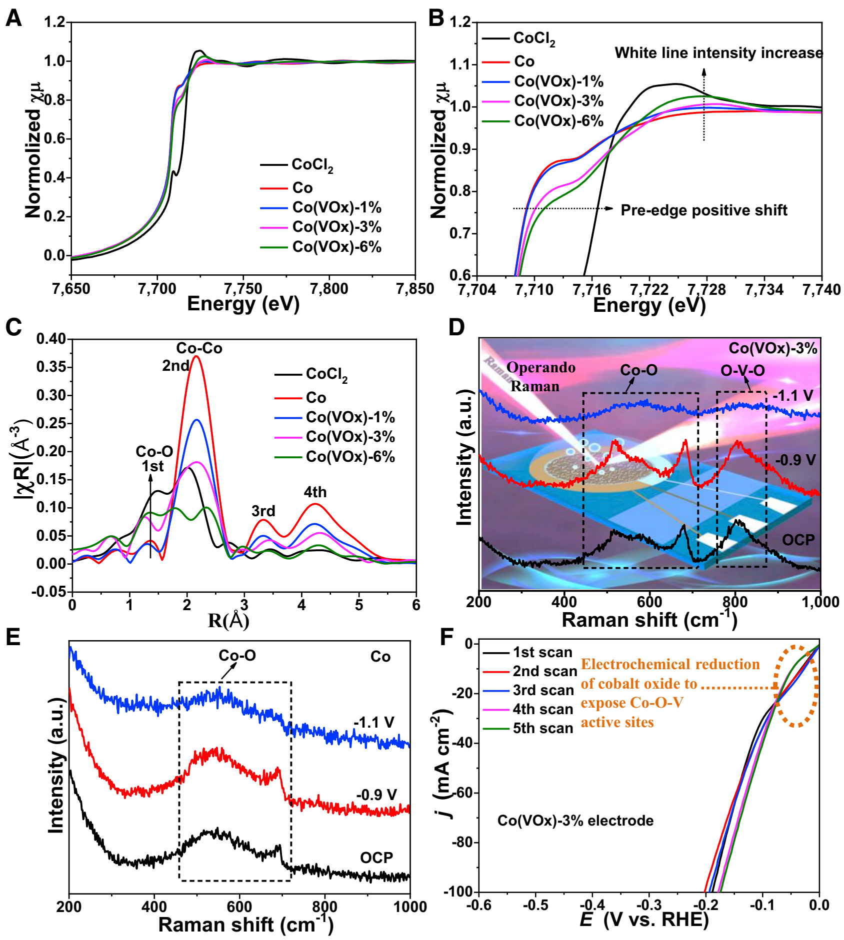

Figure 3. XAS and Operando Raman Spectra

(A and B) Co K-edge XANES spectra; (B) is an enlarged image of (A).

(C) Co K-edge FT-EXAFS of the prepared samples.

(D and E) Operando Raman spectra on Co(VOx)-3% and Co electrodes; the background schematic in (D) is the operando Raman feature by using screen-printed electrode (SPE) electrode. OCP, open circuit potential.

(F) The first 5 LSV polarization curves on the Co(VOx)-3% electrode.

surface-sensitive technique, whereas XAS is designed for bulk-averaged atom-atom correlation information. With the increment in VOx doping, the significantly reduced intensity amplitude for Co(VOx)-3% and Co(VOx)-6% demonstrates the existence of an abundant disordered structure. Furthermore, the increased 1st NN shell intensity reveals the higher oxidation degree, whereas the decreased 2nd–4th NN shell intensity indicates a much less efficient atomic packing and a greater structural disorder of metallic Co due to the regulation effect of VOx, which corresponds well to the XRD and XPS results.

Ex situ experiments yield valuable information on the chemical nature of Co(VOx); yet, the origin of catalytic activity in these NPs remains largely unknown. To address this issue, operando Raman spectroscopic experiments were performed to detect structural changes during HER conditions. To conduct operando experiments, the catalyst was held at the applying potential for 10 min before acquiring the spectrum on Co(VOx)-3% and Co electrodes. As shown in Figure 3D, several intense peaks are observed at 518 cm^{-1}, 679 cm^{-1}, and 806 cm^{-1} on Co(VOx)-3% under open circuit potential (OCP). The detected bands at 518 cm^{-1} and 679 cm^{-1} are assigned to Co oxide, which correspond to F^1_{2g} and A_{1g} vibrations, respectively.[34] The Raman peak at 806 cm^{-1} is attributed to O-V-O stretching vibrations. As the potential was increased to more negative values, e.g., −1.1 V, the vibration band peak at 679 cm^{-1} almost disappeared, whereas the characteristic peak at 518 cm^{-1} weakened, which is attributed to the reduction of the Co oxide layer. The intensity of the VOx peak at 806 cm^{-1} was also decreased, which is mainly due to the dissolution of loosely bonded or physically adsorbed VOx in KOH. It should be noted that the Co-O-V features cannot be totally removed, as the peak at 806 cm^{-1} remains with increasing the overpotential. This is further evidenced by the inductively coupled plasma optical emission spectroscopy (ICP-OES) analysis (V/Co = 2.7% for fresh sample versus V/Co = 1.4% after stability) as well as the V/Co atomic ratio of 1.2% from TEM-elemental spectra (Figure S9F) after long-term stability test. In addition, the operando Raman spectra of the pure Co electrode shows two well-defined Raman peaks at 523 cm^{-1} and 691 cm^{-1} for Co oxide under the OCP condition (Figure 3E). However, the peak intensities are much lower than those of the Co(VOx)-3% NPs, and a similar trend for the reduction of the Co oxides can be found when higher negative potentials are applied.

From the above results, it can be concluded that under HER conditions, Co oxides are first reduced to expose Co-O-V active sites to electrolyte for H_2 evolution. This is further proven by applying a negative potential at different LSV cycles on the Co(VOx)-3% electrode, for which a profound Co oxide reduction peak was observed during the first 3 cycles (Figure 3F), demonstrating the fast reduction of Co oxide for the exposure of Co-O-V active sites toward HER. It is noted that the developed electrodeposition approach can be easily extended to other conductive substrates, such as carbon fiber paper and copper foam. As seen from Figure S13, similar performances were achieved as those on the NF substrate, where the Co(VOx) electrode always shows a significantly enhanced HER activity compared with the electrodeposited bare Co electrode, demonstrating this is a general synthetic approach to fabricate active Co(VOx) electrodes on conductive substrates.

DFT Calculations

Understanding the doping effect of the oxidized V (VO_4 cluster) on the HER activity on Co(001) catalysts as the determined structure of the catalysts was followed by a series of DFT calculations to elucidate the HER on Co(001) and V-doped Co(001) (V-Co(001)) catalysts under different VO_4 coverage levels (θ = 0.25, 0.50, and 0.75). The structural model of bare Co(001) was constructed as a 4 × 4 periodic supercell (Figure S14). We considered the key reaction steps in alkaline HER, including the water dissociation reaction and the adsorption/combination of reaction H intermediates (H*). Figure S15 shows the calculated reaction energy diagram of water dissociation on Co(001) and V-Co(001) (θ = 0.25). The energy barriers for water dissociation are similar on these two surfaces (0.90 eV and 1.01 eV on Co(001) and V-Co(001) (θ = 0.25), respectively), which are quite smaller than those for other active catalysts for alkaline HER, such as $Ni_2P/NiTe_2$.[7] These results indicate that the water can be efficiently dissociated on both Co(001) and V-Co(001) surfaces with similar energy barriers.

Then, we considered all possible adsorption sites for H* closed to the VO_4 cluster (Figure S16) and all possible stable structures of V-Co(001) with $\theta \geq 0.50$ (Figures S17 and S19). Figure 4D shows the calculated free energy diagram for HER on bare Co(001), V-Co(001) (θ = 0.25-0.75), and V-Co(001) (θ = 0.50) with the highest HER activities, which are shown in Figures 4A, 4B, S18, and S20. For the bare Co(001), the ΔG_{H^*} is highly negative (−0.32 eV), which indicates a strong interaction

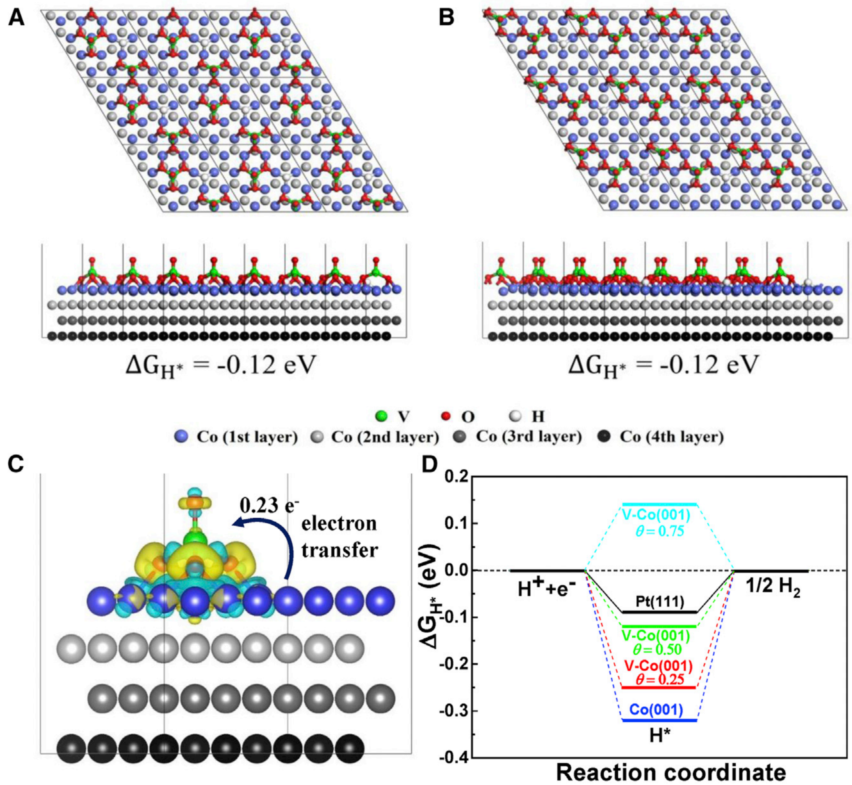

Figure 4. DFT Simulation on the Origin of the Enhanced HER Activity

(A and B) Top (top) and side (bottom) views of the optimized structures of H* adsorbed on V-Co(001) (θ = 0.50) with the highest HER activity. The corresponding ΔG_{H^*} are listed below the panels.

(C) The deformation electronic density of V-Co(001) (θ = 0.25). Yellow and cyan refer to electron-rich and -deficient areas, respectively. The isosurface value is 0.004 e Å^{-3}.

(D) The calculated ΔG_{H^*} diagram of the HER at the equilibrium potential for various Co(001)-based catalysts. The values for Pt(111) are also shown for comparison.

between H* and Co(001),[35] manifesting poor HER reaction kinetics. Introducing a low coverage of the VO_4 cluster on Co(001), namely V-Co(001) (θ = 0.25), significantly increased the value of ΔG_{H^*} to −0.25 eV, suggesting an enhanced HER activity compared to bare Co(001). The deformation electronic density calculation (Figures 4C and S21) and Bader analysis show that the VO_4 cluster has led to an increase in electronic charge density on VO_4 and a loss of electron charge density on the surrounding six Co atoms, and there are 0.23 electrons transferred from each Co to VO_4 based on the Bader analysis. Fewer electrons localized on Co sites closest to VO_4 results in the weak H adsorption on V-Co(001) and thus the enhanced HER activity. Moreover, we found that a further increase of the coverage of VO_4 clusters on the Co(001) surface can further increase the values of ΔG_{H^*}. For example, the ΔG_{H^*} for V-Co(001) (θ = 0.50) and V-Co(001) (θ = 0.75) are −0.12 eV and 0.14 eV, respectively. These results indicate that the HER activities of V-Co(001) with a high VO_4 coverage (θ ≥ 0.50) are much higher than those with low VO_4 coverage (θ ≤ 0.25). In addition, considering that the number of active sites for V-Co(001) (θ = 0.75) (Figure S20) are fewer than those of V-Co(001) (θ = 0.50) (Figure S18), we conclude the HER activity follows the order of V-Co(001) (θ = 0.50) > V-Co(001) (θ = 0.75) > V-Co(001) (θ = 0.25) > Co(001), which is consistent with experimental results. It has to be noted that the binding of reaction intermediates on low-coordinated metal atoms is stronger than that on high-coordinated metal sites.[36] The small particle size of Co can significantly increase the proportion of low-coordinated metal atoms, such as step atoms, kink atoms, and vacancies, which can increase the binding strength of H*. Hence, the absolute value of adsorption energy of H* should be decreased as Co particle size increases. In other words, the downsized Co NPs should have a stronger H* adsorption and decrease HER activity. Although the downsized Co particle itself has a strong H* adsorption energy, for our developed Co(VOx) catalyst, the VOx modification can significantly decrease the H* adsorption energy compared with that of bare Co, thus leading to the excellent HER performances.

In summary, a Co(VOx) catalyst was developed with a refined NP size, disordered structure, and a significantly enhanced alkaline H_2 evolution activity. The best Co(VOx) electrode can only be achieved at appropriate VOx doping levels to offer suitable H binding as well as abundant active sites during HER. This study provides a promising approach for achieving notable HER performance with metallic Co, which is known to be a poor catalyst for HER, and sheds light on the crucial role of atomic structure modification through a facile VOx engineering strategy. The development of highly active metallic Co-based catalysts for HER would find applications in the water electrolysis industry and also potentially provide a multifunctional catalyst for the FTS industry for which metallic Co is currently most widely used for the synthesis of valuable long-chain hydrocarbons from H_2 and carbon monoxide. The proposed approach can also be potentially extended to other non-active metallic Fe triad materials for developing efficient low-cost electrocatalysts for H_2 production.

EXPERIMENTAL PROCEDURES

Resource Availability

Lead Contact

Further information and requests for resources should be directed to the Lead Contact, Prof. Chuan Zhao (chuan.zhao@unsw.edu.au).

Materials Availability

This study did not generate new unique materials.

Data and Code Availability

The authors declare that data supporting the findings of this study are available within the article and the Supplemental Experimental Procedures. All other data are available from the lead contact upon reasonable request.

Preparation of the Co(VOx) Electrode

The Co(VOx) electrodes were prepared by a direct electrodeposition approach in a three-electrode system with the NF as the working electrode, graphite plate as the counter electrode, and a double junction saturated calomel electrode (SCE) as the reference electrode. The NF was cleaned in a 5 M HCl solution for 10 min and rinsed Milli-Q water before use. The electrodeposition was carried out in an electrolyte consisting of 0.45 M $CoCl_2 \cdot 6H_2O$, 4.5 to 27 mM (V/Co = 0%–6%) NH_4VO_3, and 0.35 M H_3BO_3, by dissolving the chemicals in 50 mL Milli-Q water under sonication. The electrodeposition was performed on a CHI 760D electrochemical workstation at −1.9 V (versus SCE) for 600 s. The Co(VOx) mass loading on NF was 2.3 ± 0.4 mg cm^{-2}. The preparation of other control samples can be found in detail in the Supplemental Experimental Procedures.

Electrochemical Measurement

All the electrochemical measurements were carried out on a CHI 760D electrochemical workstation by using the prepared Co(VOx) and Co electrodes on NF as the working electrode and graphite plate and double junction SCE (saturated KCl) as the counter and reference electrode, respectively. All potentials measured were calibrated to the reversible H_2 electrode (RHE) through the following equation: E_{RHE} = E_{SCE} + 0.241 V + 0.059 pH. The linear sweep voltammetry (LSV) polarization curves were recorded at a scan rate of 3 mV s^{-1} in 1 M KOH without iR compensation. Chronoamperometric measurements were obtained under the same experimental setup. EIS spectra were measured at 150 mV overpotential in the frequency range of 0.1–100000 Hz with an amplitude of 10 mV in 1 M KOH electrolyte.

DFT Calculations

All of the spin-polarized DFT calculations were performed using the vienna Ab initio simulation package (VASP) program,[37–39] which uses a plane-wave basis set and a projector augmented wave method (PAW) for the treatment of core electrons. The Perdew, Burke, and Ernzerhof exchange-correlation functional within a generalized gradient approximation (GGA-PBE)[40] was used in our calculations. For the expansion of wave functions over the plane-wave basis set, a converged cutoff was set to 450 eV. Spin-polarization effect and dipole correction were considered in all cases.

The structural model of bare Co(001) was constructed as a 4 × 4 periodic supercell (Figure S14A), which contains four atomic layers with the bottom two layers fixed in their respective bulk positions and all the other atoms fully relaxed. Experimental observations show that V-dopant atoms are oxidized and adsorb on the Co(001) surface. In order to simulate V-doped Co(001) catalysts, VO_4 clusters are added to the Co(001) surface to model V-doped Co(001) catalysts with different VO_4 coverages (V-Co(001) (θ = 0.25, 0.50 and 0.75)). For example, Figure S14B shows the simulation model of V-Co(001) (θ = 0.25). The vacuum space was set to larger than 18 Å in the z direction to avoid interactions between periodic images. In geometry optimizations, all the structures were relaxed up to the residual atomic forces smaller than 0.005 eV/Å, and the total energy was converged to 10^{-4} eV. The Brillouin zone was sampled using 3 × 3 × 1 Γ-centered mesh. The deformation electronic density of the V-Co(001) was defined as $\Delta\rho(r) = \rho(r)_{V-Co(001)} - \rho(r)_{Co(001)} - \rho(r)_{VO_4}$, where $\rho(r)_{V-Co(001)}$ represent the charge density of the V-Co(001) system, and $\rho(r)_{Co(001)}$ and $\rho(r)_{VO_4}$ represent the charge density of the bare Co(001) and the VO_4 cluster at the same coordinates as those in the V-Co(001) system, respectively.

The overall HER mechanism was evaluated with a three-state diagram consisting of an initial H^+ state, an intermediate H* state, and 1/2 H_2 as the final product. The free energy of H* (ΔG_{H^*}) is proven to be a key descriptor to characterize the HER activity of the electrocatalyst. A electrocatalyst with a positive value leads to low kinetics of adsorption of H, whereas a catalyst with a negative value leads to low kinetics of release of H_2 molecules.[35] The optimum value of $|\Delta G_{H^*}|$ should be zero; for instance, this value for the well-known highly efficient Pt catalyst is near zero as $|\Delta G_{H^*}| \approx 0.09$ eV.[5] The ΔG_{H^*} is calculated as[35]

$$\Delta G_{H^*} = \Delta E_{H^*} + \Delta E_{ZPE} - T\Delta S_H \quad \text{(Equation 1)}$$

where ΔE_{H^*} is the binding energy of adsorbed H and ΔE_{ZPE} and ΔS_H are the difference in zero point energy (ZPE) and entropy between the adsorbed H and H_2 in the gas phase, respectively. As the contribution from the vibrational entropy of H in the adsorbed state is negligibly small, the entropy of H adsorption is $\Delta S_H \approx -1/2 S_{H_2}$, where S_{H_2} is the entropy of H_2 in the gas phase at the standard conditions. Therefore, the ΔG_{H^*} value for the Co(001) surface should be $\Delta E_H + 0.24$ eV.[35]

Other Characterizations

More details of the characterization methods followed, XAS data collection, and operando Raman measurements are provided in Supplemental Experimental Procedures.

SUPPLEMENTAL INFORMATION

Supplemental Information can be found online at https://doi.org/10.1016/j.xcrp.2020.100275.

ACKNOWLEDGMENTS

All physical characterizations were carried out at the Mark Wainwright Analytical Centre (MWAC) and Electron Microscope Unit at the University of New South Wales (UNSW). XAS spectra were recorded on the multiple wiggler XAS beamline 12 ID at the Australian Synchrotron (AS1/XAS/15778). Thanks to Dr. Hangjuan Ren for the schematic drawing. Thanks to Dr. Rosalie Hocking at Swinburne University of Technology and Dr. Bernt Johannessen at Australian Synchrotron for the help of XAS data collection. Thanks to Mr. Kamran Dastafkan for proofreading the paper. This research was undertaken with the assistance of resources provided by the Pawsey and the National Computational Infrastructure (NCI) facilities at the Australian National University, which were allocated through the National Computational Merit Allocation Scheme and supported by the Australian Government and the Australian Research Council grant (LE190100021). C.Z. is grateful for the award of a Future Fellow from Australian Research Council (FT170100224).

AUTHOR CONTRIBUTIONS

C.Z. and Y.L. designed the experiments. Y.L. undertook electrochemical experiments; performed the XRD, TEM, and XAS; and interpreted data. X.T. and S.C.S. undertook the DFT calculation. W.Y. collected the Faradic efficiency data, X.B. helped to collect the XAS data, Z.S. performed XPS, and T.Z. collected SEM. C.Z., Y.L., X.T., and S.C.S. co-wrote the paper. All authors discussed the results and commented on the manuscript.

DECLARATION OF INTERESTS

The authors declare no competing interests.

Received: September 14, 2020
Revised: October 22, 2020
Accepted: November 6, 2020
Published: December 23, 2020

REFERENCES

1. Walter, M.G., Warren, E.L., McKone, J.R., Boettcher, S.W., Mi, Q., Santori, E.A., and Lewis, N.S. (2010). Solar water splitting cells. Chem. Rev. *110*, 6446–6473.
2. Suryanto, B.H.R., Wang, Y., Hocking, R.K., Adamson, W., and Zhao, C. (2019). Overall electrochemical splitting of water at the heterogeneous interface of nickel and iron oxide. Nat. Commun. *10*, 5599.
3. Wang, Y., Arandiyan, H., Dastafkan, K., Li, Y.B., and Zhao, C. (2020). Common pitfalls of reporting electrocatalysts for water splitting. Chem. Res. Chin. Univ. *36*, 360–365.
4. Li, Y., and Zhao, C. (2017). Enhancing water oxidation catalysis on a synergistic phosphorylated NiFe hydroxide by adjusting catalyst wettability. ACS Catal. *7*, 2535–2541.
5. Zheng, Y., Jiao, Y., Jaroniec, M., and Qiao, S.Z. (2015). Advancing the electrochemistry of the hydrogen-evolution reaction through combining experiment and theory. Angew. Chem. Int. Ed. Engl. *54*, 52–65.
6. Li, Y., and Zhao, C. (2016). Iron-doped nickel phosphate as synergistic electrocatalyst for water oxidation. Chem. Mater. *28*, 5659–5666.

7. Li, Y., Tan, X., Tan, H., Ren, H.J., Chen, S., Yang, W.F., Smith, S.C., and Zhao, C. (2020). Phosphine vapor-assisted construction of heterostructured $Ni_2P/NiTe_2$ catalysts for efficient hydrogen evolution. Energy Environ. Sci. *13*, 1799–1807.

8. Li, Y., Tan, X., Hocking, R.K., Bo, X., Ren, H., Johannessen, B., Smith, S.C., and Zhao, C. (2020). Implanting Ni-O-VOx sites into Cu-doped Ni for low-overpotential alkaline hydrogen evolution. Nat. Commun. *11*, 2720.

9. Zhu, Z., Yin, H., He, C.T., Al-Mamun, M., Liu, P., Jiang, L., Zhao, Y., Wang, Y., Yang, H.G., Tang, Z., et al. (2018). Ultrathin transition metal dichalcogenide/3d metal hydroxide hybridized nanosheets to enhance hydrogen evolution activity. Adv. Mater. *30*, e1801171.

10. Zhuang, Z., Li, Y., Li, Z., Lv, F., Lang, Z., Zhao, K., Zhou, L., Moskaleva, L., Guo, S., and Mai, L. (2018). MoB/g-C_3N_4 interface materials as a schottky catalyst to boost hydrogen evolution. Angew. Chem. Int. Ed. Engl. *57*, 496–500.

11. Li, Y., Tan, X., Chen, S., Bo, X., Ren, H., Smith, S.C., and Zhao, C. (2019). Processable surface modification of nickel-heteroatom (N, S) bridge sites for promoted alkaline hydrogen evolution. Angew. Chem. Int. Ed. Engl. *58*, 461–466.

12. Lei, Z., Bai, J., Li, Y., Wang, Z., and Zhao, C. (2017). Fabrication of nanoporous nickel-iron hydroxylphosphate composite as bifunctional and reversible catalyst for highly efficient intermittent water splitting. ACS Appl. Mater. Interfaces *9*, 35837–35846.

13. Sun, Q., Dong, Y., Wang, Z., Yin, S., and Zhao, C. (2018). Synergistic nanotubular copper-doped nickel catalysts for hydrogen evolution reactions. Small *14*, e1704137.

14. Wang, H., Xiao, X., Liu, S., Chiang, C.L., Kuai, X., Peng, C.K., Lin, Y.C., Meng, X., Zhao, J., Choi, J., et al. (2019). Structural and electronic optimization of MoS_2 edges for hydrogen evolution. J. Am. Chem. Soc. *141*, 18578–18584.

15. Greeley, J., Jaramillo, T.F., Bonde, J., Chorkendorff, I.B., and Nørskov, J.K. (2006). Computational high-throughput screening of electrocatalytic materials for hydrogen evolution. Nat. Mater. *5*, 909–913.

16. Kuang, Y., Feng, G., Li, P., Bi, Y., Li, Y., and Sun, X. (2016). Single-crystalline ultrathin nickel nanosheets array from in situ topotactic reduction for active and stable electrocatalysis. Angew. Chem. Int. Ed. Engl. *55*, 693–697.

17. Tasker, S.Z., Standley, E.A., and Jamison, T.F. (2014). Recent advances in homogeneous nickel catalysis. Nature *509*, 299–309.

18. Hudson, R., Hamasaka, G., Osako, T., Yamada, Y.M.A., Li, C.J., Uozumi, Y., and Moores, A. (2013). Highly efficient iron(0) nanoparticle-catalyzed hydrogenation in water in flow. Green Chem. *15*, 2141–2148.

19. Liu, J.X., Su, H.Y., Sun, D.P., Zhang, B.Y., and Li, W.X. (2013). Crystallographic dependence of CO activation on cobalt catalysts: HCP versus FCC. J. Am. Chem. Soc. *135*, 16284–16287.

20. Cheng, Q., Tian, Y., Lyu, S., Zhao, N., Ma, K., Ding, T., Jiang, Z., Wang, L., Zhang, J., Zheng, L., et al. (2018). Confined small-sized cobalt catalysts stimulate carbon-chain growth reversely by modifying ASF law of Fischer-Tropsch synthesis. Nat. Commun. *9*, 3250.

21. Kong, D., Wang, H., Lu, Z., and Cui, Y. (2014). $CoSe_2$ nanoparticles grown on carbon fiber paper: an efficient and stable electrocatalyst for hydrogen evolution reaction. J. Am. Chem. Soc. *136*, 4897–4900.

22. Wang, Y., Liu, D., Liu, Z., Xie, C., Huo, J., and Wang, S. (2016). Porous cobalt-iron nitride nanowires as excellent bifunctional electrocatalysts for overall water splitting. Chem. Commun. (Camb.) *52*, 12614–12617.

23. Zu, M.Y., Liu, P.F., Wang, C.W., Wang, Y., Zheng, L.R., Zhang, B., Zhao, H.J., and Yang, H.G. (2018). Bimetallic carbide as a stable hydrogen evolution catalyst in harsh acidic water. ACS Energy Lett. *3*, 78–84.

24. King, L.A., Hubert, M.A., Capuano, C., Manco, J., Danilovic, N., Valle, E., Hellstern, T.R., Ayers, K., and Jaramillo, T.F. (2019). A non-precious metal hydrogen catalyst in a commercial polymer electrolyte membrane electrolyser. Nat. Nanotechnol. *14*, 1071–1074.

25. Marinescu, S.C., Winkler, J.R., and Gray, H.B. (2012). Molecular mechanisms of cobalt-catalyzed hydrogen evolution. Proc. Natl. Acad. Sci. USA *109*, 15127–15131.

26. Sun, T., Zhao, S., Chen, W., Zhai, D., Dong, J., Wang, Y., Zhang, S., Han, A., Gu, L., Yu, R., et al. (2018). Single-atomic cobalt sites embedded in hierarchically ordered porous nitrogen-doped carbon as a superior bifunctional electrocatalyst. Proc. Natl. Acad. Sci. USA *115*, 12692–12697.

27. Qin, C., Hou, B., Wang, J.G., Wang, Q., Wang, G., Yu, M.T., Chen, C.B., Jia, L.T., and Li, D.B. (2018). Crystal-plane-dependent Fischer-Tropsch performance of cobalt catalysts. ACS Catal. *8*, 9447–9455.

28. Harmel, J., Peres, L., Estrader, M., Berliet, A., Maury, S., Fécant, A., Chaudret, B., Serp, P., and Soulantica, K. (2018). Hcp-Co nanowires grown on metallic foams as catalysts for Fischer–Tropsch synthesis. Angew. Chem. Int. Ed. Engl. *57*, 10579–10583.

29. McDonald, K.J., and Choi, K.-S. (2011). Photodeposition of Co-based oxygen evolution catalysts on alpha-Fe_2O_3 photoanodes. Chem. Mater. *23*, 1686–1693.

30. Hess, C., Tzolova-Muller, G., and Herbert, R. (2007). The influence of water on the dispersion of vanadia supported on silica SBA-15: A combined XPS and raman study. J. Phys. Chem. C *111*, 9471–9479.

31. Liu, T., Liu, D., Qu, F., Wang, D., Zhang, L., Ge, R., Hao, S., Ma, Y., Du, G., Asiri, A.M., et al. (2017). Enhanced electrocatalysis for energy-efficient hydrogen production over CoP catalyst with nonelectroactive Zn as a promoter. Adv. Energy Mater. *7*, 1700020.

32. McCrory, C.C.L., Jung, S., Peters, J.C., and Jaramillo, T.F. (2013). Benchmarking heterogeneous electrocatalysts for the oxygen evolution reaction. J. Am. Chem. Soc. *135*, 16977–16987.

33. King, H.J., Bonke, S.A., Chang, S.L.Y., Spiccia, L., Johannessen, B., and Hocking, R.K. (2017). Engineering disorder into heterogenite-like cobalt oxides by phosphate doping: implications for the design of water-oxidation catalysts. ChemCatChem *9*, 511–521.

34. Louardi, A., Rmili, A., Ouachtari, F., Bouaoud, A., Elidrissi, B., and Erguig, H. (2011). Characterization of cobalt oxide thin films prepared by a facile spray pyrolysis technique using perfume atomizer. J. Alloys Compd. *509*, 9183–9189.

35. Norskov, J.K., Bligaard, T., Logadottir, A., Kitchin, J.R., Chen, J.G., Pandelov, S., and Norskov, J.K. (2005). Trends in the exchange current for hydrogen evolution. J. Electrochem. Soc. *152*, J23–J26.

36. Zhang, K., Guo, R., Pang, F., He, J., and Zhang, W. (2019). Low-Coordinated Gold Atoms Boost Electrochemical Nitrogen Reduction Reaction under Ambient Conditions. ACS Sustain. Chem. Eng. *7*, 10214–10220.

37. Kresse, G., and Hafner, J. (1994). Ab initio molecular-dynamics simulation of the liquid-metal-amorphous-semiconductor transition in germanium. Phys. Rev. B Condens. Matter *49*, 14251–14269.

38. Kresse, G., and Joubert, D. (1999). From ultrasoft pseudopotentials to the projector augmented-wave method. Phys. Rev. B Condens. Matter Mater. Phys. *59*, 1758–1775.

39. Kresse, G., and Furthmüller, J. (1996). Efficient iterative schemes for ab initio total-energy calculations using a plane-wave basis set. Phys. Rev. B Condens. Matter *54*, 11169–11186.

40. Perdew, J.P., Burke, K., and Ernzerhof, M. (1996). Generalized gradient approximation made simple. Phys. Rev. Lett. *77*, 3865–3868.